PHYSICAL REVIEW B **104**, 195108 (2021)

Anomalous Hall effect from gapped nodal line in the Co_2FeGe Heusler compound

Gaurav K. Shukla,[1] Jyotirmoy Sau,[2] Nisha Shahi,[1] Anupam K. Singh,[1] Manoranjan Kumar,[2] and Sanjay Singh[1,*]

[1] *School of Materials Science and Technology, Indian Institute of Technology (Banaras Hindu University), Varanasi 221005, India*

[2] *S. N. Bose National Centre for Basic Sciences, Kolkata 700098, West Bengal, India*

(Received 1 June 2021; revised 21 September 2021; accepted 19 October 2021; published 5 November 2021)

Full Heusler compounds with cobalt as a primary element show anomalous transport properties owing to the Weyl fermions and broken time-reversal symmetry. We present here the study of anomalous Hall effect (AHE) in the Co_2FeGe Heusler compound. The experiment reveals anomalous Hall conductivity (AHC) ~100 S/cm at room temperature with an intrinsic contribution of ~78 S/cm. The analysis of anomalous Hall resistivity suggests the scattering independent intrinsic mechanism dominates the overall behavior of anomalous Hall resistivity. The first principles calculation reveals that the Berry curvature originated by a gapped nodal line near E_F is the main source of AHE in the Co_2FeGe Heusler compound. The theoretically calculated AHC is in agreement with the experiment.

DOI: 10.1103/PhysRevB.104.195108

I. INTRODUCTION

Weyl semimetals (WSMs) host exotic transport properties resulting from their nontrivial topological band structure [1–6]. WSMs are characterized by chiral anomaly and linear band crossing points known as Weyl points or Weyl nodes [7]. The existence of Weyl nodes are possible in metal or semimetal with broken inversion symmetry (IS) and/or time reversal symmetry (TRS). These broken symmetries lift the twofold degeneracy of electronic bands in the framework of Kramer's theorem [8] and the linearly dispersing touching points of two nondegenerate bands become Weyl points [9,10]. The Hamiltonian of the system describing Weyl nodes can be written in terms of the basis vector of three Pauli matrices and hence any perturbation with linear combination of Pauli matrices cannot destroy the Weyl nodes [9]. Also no other symmetries are required (except translational symmetry) for the protection of Weyl nodes that represent the Weyl nodes as topologically stable objects [11]. Berry introduced the concept of Berry curvature [12] which may be mapped to a pseudomagnetic field and the degenerate Weyl points correspond to quantized monopoles that form source and sink of Berry curvature. These concepts help us to understand the various intriguing phenomena like anomalous Hall effect (AHE) [13,14], anomalous Nernst effect (ANE) [15], chiral magnetoresistance [2,7], second harmonic generation [2], etc. Weyl points induced by the breaking of IS were observed experimentally the first time in TaAs [16–18] and investigated extensively in its family members [19,20] and also in other materials [21–23]. TRS breaking WSMs are also known as magnetic WSMs discovered very recently and created much interest due to exhibiting large intrinsic AHE and anomalous Hall conductivity (AHC), which is proportional to the separation of Weyl nodes [13,24,25]. The magnetic WSMs have an added advantage over conventional WSMs because an external magnetic field can be used to manipulate the properties of magnetic WSMs [26]. Co_3SnS_2, a ferromagnet kagome lattice, was first discovered as magnetic WSM exhibits a large Berry curvature resulting in the giant intrinsic AHC 1130 S/cm, which is an order of magnitude larger than the typical ferromagnets [27]. This large Berry curvature attributes to the presence of Weyl nodes and nodal rings of linear crossings in the spin-up channel based on band inversion. Besides Co_3SnS_2, several other materials such as pyrochlore iridates [28–30], PrAlGe [26], $YMnBi_2$ [31], Mn_3Sn [32], $Co_3MM'X_2$ (M/M' = Ge, Sn, Pb; X = S, Se, Te) [33], and Heusler alloys [24,34–37] have been identified as magnetic WSMs theoretically and/or experimentally.

Among various magnetic WSM candidates, Co_2-based Heusler compounds have been found to be more interesting which drives the large AHC due to a large Berry curvature [24,34,35,38]. In most of the Co_2-based magnetic WSMs, a gapped nodal line in momentum space has been found as a major source of Berry curvature and creates intrinsic AHE [24,39,40]. In these compounds, three gapless nodal lines which are protected by three mirror planes exist in the absence of magnetization. The gapless nodal line gaps out with the introduction of spin orbit coupling (SOC) according to the magnetization direction [13,39]. For example, Co_2MnGa exhibits a giant AHC around 1260 S/cm at 60 K due to large Berry curvature associated with the gapped nodal line [40]. Co_2VGa exhibit the AHC around 140 S/cm due to a slight gapped nodal line result from reduced mirror symmetry upon introducing magnetization [14]. Recently, the Co_2MnAl Weyl semimetal is reported to have large AHC 1600 S/cm at 2 K due to a gapped nodal ring in momentum space, which is as large as for 3D quantum AHE [24].

Theoretical investigation performed on the Co_2FeGe Heusler compound reveals the existence of a nodal line above the Fermi energy (E_F) results in an intrinsic AHE [15,41]. In this manuscript, we present a study of AHE on the Co_2FeGe Heusler compound using both experiment and theoretical calculations. We found the experimental AHC ~ 100 S/cm at

---

[*] ssingh.mst@iitbhu.ac.in

300 K and shows weak dependence on temperature. Our first principles calculation reveals that the magnetization induced gapped nodal line near the E_F is the main source of AHE in Co_2FeGe.

II. METHODS

The polycrystalline Co_2FeGe compound was synthesized by a standard arc melting technique [42] in the presence of pure argon atmosphere using 99.99% pure individual elements. The sample was remelted several times for the homogeneous mixing of involved elements. A small weight loss of 0.62% was notified after melting. A small piece was taken from a sample and crushed into powder for x-ray diffraction measurement. The polished rectangular piece of the dimension $4 \times 2 \times 0.65$ mm^3 was used for temperature and magnetic field dependent transport measurements using a cryogen free measurement system (Cryogenic, CFMS). To obtain the actual transverse resistivity (ρ_H), raw Hall resistivity data (${\rho_H}^{\text{raw}}$) was antisymmetrized by averaging the difference of ${\rho_H}^{\text{raw}}$ at the positive field and negative field with respect to the field sweep direction.

The electronic band structure and magnetic properties of the Co_2FeGe are calculated employing density functional theory (DFT) using the Vienna ab initio simulation package (VASP) [43]. Exchange-correlation potential is approximated with generalized gradient approximation and the projector augmented wave method (PAW) [44] is used for core-valence interaction. The calculations are performed with K mesh of $10 \times 10 \times 10$ for the $Fm\bar{3}m$ space group (space group no. 225). The plane-wave basis is used with cutoff energy 500 eV and force convergence for the optimization is kept below 0.001 eV/Å. Self-consistent calculations are performed to get the charge density and thereafter the band structure is calculated. To understand the DFT band structure, Wannier interpolated bands and corresponding tight-binding parameters are calculated using Wannier90 [45,46]. The anomalous Hall conductivity (AHC), Berry curvature, and energy gap for the given parameters are calculated using the WANNIERTOOL [47]. For AHC calculation Kubo formalism is used in the clean limit [48]. Co_2FeGe material possess $Fm\bar{3}m$ symmetry and have three relevant mirror planes, $m_x(k_x{=}0)$, $m_y(k_y{=}0)$, and $m_z(k_z{=}0)$, and three C_4 rotation axes, k_x, k_y, and k_z [35]. The magnetization is oriented along the z axis and the SOC is also considered along the same axis.

III. RESULTS AND DISCUSSION

A. Structural analysis

The x-ray diffraction (XRD) pattern of the sample collected at room temperature is for structural investigation and phase purity. The Rietveld analysis of the XRD pattern was done using FULLPROF software [49]. The space group $Fm\bar{3}m$ and Wyckoff positions 8c (1/4, 1/4, 1/4), occupied by Co atoms, and 4b (1/2, 1/2, 1/2) and 4a (0, 0, 0), occupied by Fe and Ge atoms, respectively, were used. The observed XRD patterns depicted in Fig. 1(a) show that all the Bragg peaks observed are well indexed, confirming the phase purity (cubic) of the Co_2FeGe sample. The refined unit cell parameter was found to be 5.74 Å.

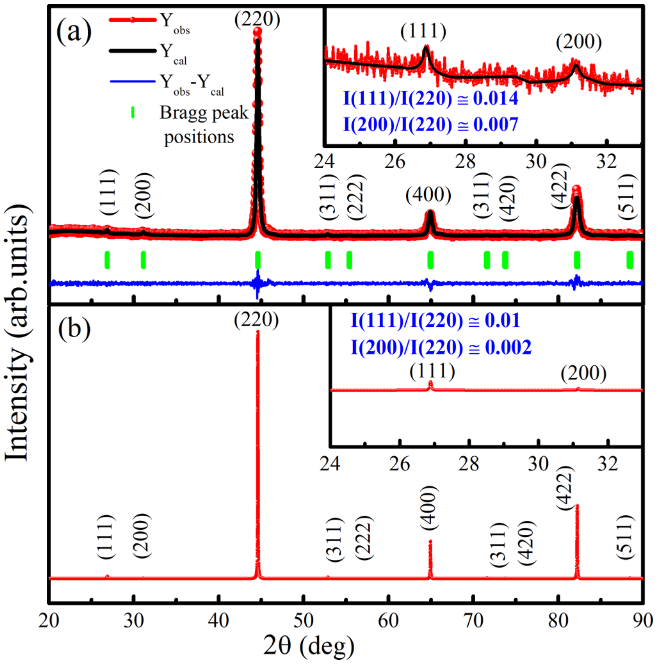

FIG. 1. (a) Rietveld modeling of the x-ray diffraction (XRD) pattern of Co_2FeGe at room temperature. (b) Simulated XRD pattern of Co_2FeGe. Insets of figures show the enlarged view around the (111) and (200) superlattice reflections.

For full Heusler alloys the reflections index relation h, k, and l = odd number or $(h+k+l)/2 = (2n+1)$ are the superlattice reflections, while $(h+k+l)/2 = 2n$ are the fundamental reflections [50,51]. The ordered structure of full Heusler alloys ($L2_1$ structure) generally mark the presence of (111) and (200) superlattice reflections; the presence of (111) peak indicates the chemical ordering of an atom at the octahedral position and (200) peak indicates the ordering at the tetrahedral position, while the intensity of (220) fundamental reflection is independent from atomic ordering [52]. The presence of both (111) and (200) superlattice peaks primarily suggest the $L2_1$ structure of Co_2FeGe as shown in the inset of Fig. 1(a). To compare the experimentally observed relative intensities of the superlattice reflections with theory, we simulated the XRD pattern using PowderCell software as shown in Fig. 1(b). Similar to the observed, weak intensities of (111) and (200) superlattice reflections have also been observed in a simulated XRD pattern. The enlarged view of simulated superlattice peaks is shown in the inset of Fig. 1(b). The weak intensity of superlattice reflections is due to the small difference between the atomic scattering factors of constituent 3d metals of Co_2FeGe [53,54]. The measured and simulated $\frac{I_{111}}{I_{220}}$ and $\frac{I_{200}}{I_{220}}$ are given in the insets of Figs. 1(a) and 1(b), respectively. A good match between the measured and simulated XRD patterns suggests the formation of an ordered structure of Co_2FeGe.

B. Magnetization and resistivity

Magnetic isotherms up to a field of 5 T were recorded at temperatures 2 K and 300 K depicted in Fig. 2(a).The magnetic moment was found to be 5.38μ_B/f.u. and 5.24μ_B/f.u. at 2 K and 300 K, respectively. The observed magnetic

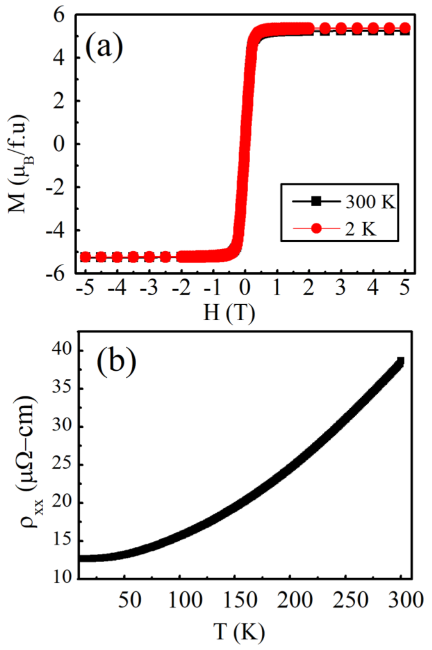

FIG. 2. (a) Field dependent magnetization curves at 2 K and 300 K. (b)Temperature dependent longitudinal resistivity ρ_{xx}.

moment is well in agreement with the literature [55,56], as well as our theoretical calculation (discussed later). The variation of longitudinal resistivity (ρ_{xx}) as a function of temperature from 10 K to 300 K is shown in Fig. 2(b). The ρ_{xx} increases with increasing temperature and a residual resistivity about 14 $\mu\Omega$ cm is observed. The nonlinear behavior of resistivity above 50 K suggests the combined phonon and magnon scattering state [57]. The residual resistance ratio [RRR = $\rho_{xx}(300\ \mathrm{K})/\rho_{xx}(10\ \mathrm{K})$] which quantifies the degree of disorder is 2.82. This value is larger than most of the Co$_2$-based Heusler alloy [39,58–61], which signifies a comparatively clean sample.

C. Anomalous Hall

After investigation of the phase purity, saturation magnetization, and temperature variation of the longitudinal resistivity, we carried out a detailed magnetotransport measurement in a wide range of temperatures 50 K to 300 K to study the AHE in the Co$_2$FeGe Heusler alloy. Hall resistivity (ρ_{H}) curves measured up to 4 T magnetic field at different temperatures are shown in Fig. 3(a). The ρ_{H} is given by the equation $\rho_H(H) = R_0H + R_sM$ [39,62], where R_0 and R_s are the normal and anomalous Hall coefficients. H is the external applied magnetic field and M is magnetization of the material. It is evident from Fig. 3(a) that ρ_{H} initially increases at lower fields indicating AHE in Co$_2$FeGe and shows the positive slope according to the sign of the ordinary Hall coefficient at a higher field region for all temperatures. The anomalous Hall resistivity (ρ_{AH}) is calculated by the zero field extrapolation of high field Hall data with the ordinate, which is equivalent to the Hall voltage response arising due to spontaneous magnetization in the absence of external magnetic field. Figure 3(b) shows the extracted ρ_{AH} versus

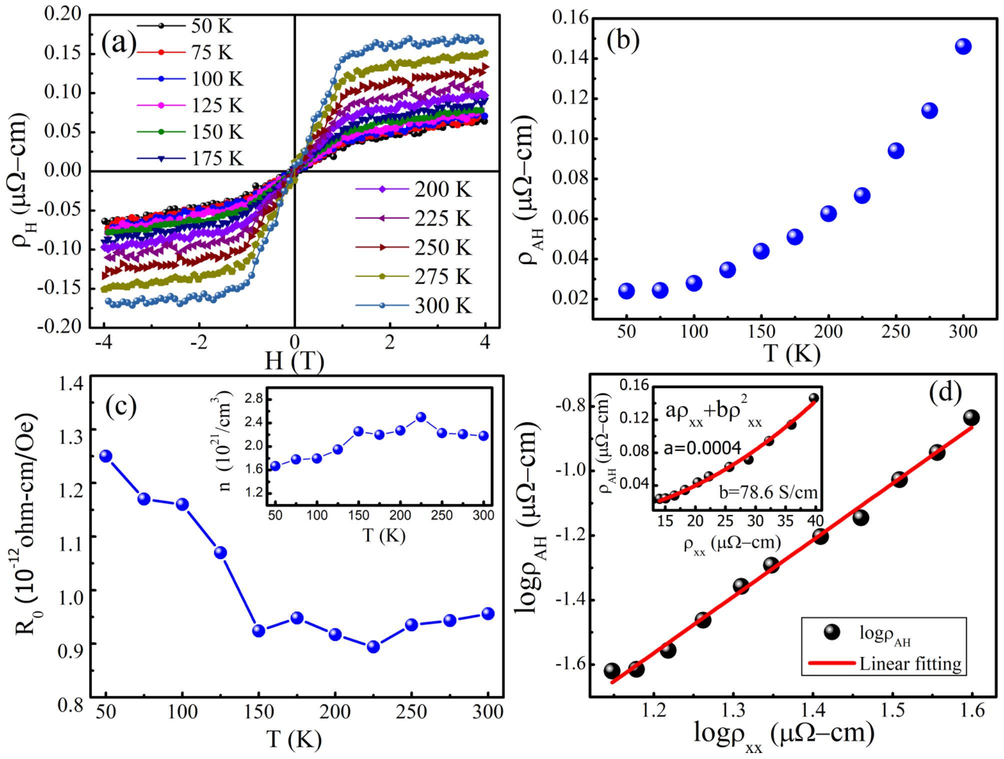

FIG. 3. (a) Field dependent Hall resistivityρ_H at indicated temperatures. (b) Temperature dependent anomalous Hall resistivity ρ_{AH}. (c) Temperature dependent normal Hall coefficient R$_0$. Inset shows the temperature dependent carrier concentration n. (d) Double logarithmic plot between ρ_{AH} and ρ_{xx} (black balls) and linear fitting is shown by red line. Inset shows the graph between ρ_{AH} and ρ_{xx} (black balls) and fitting using Eq. (1) is shown by red line.

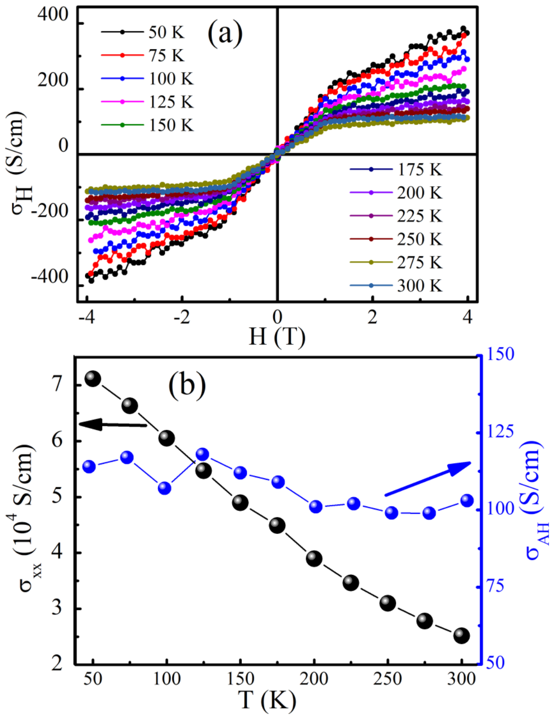

FIG. 4. (a) Field dependent Hall conductivity σ_H. (b) Temperature dependent longitudinal conductivity σ_{xx} (black spheres) and AHC (blue spheres).

temperature plot, which displays that the Hall resistivity increases with increasing temperature and acquires a maximum value of 0.14 $\mu\Omega$ cm at room temperature and a small value 0.02 $\mu\Omega$ cm at 50 K. The slope of high field Hall resistivity data gives the normal Hall coefficient (R_0) and variation of R_0 with temperature is shown in Fig. 3(c). By using relation $R_0 = \frac{1}{ne}$, we calculated carrier density (n) and plotted in the inset of Fig. 3(c) with temperature. The value of n was found to be $\sim 2 \times 10^{21}$ cm^3. The positive value of R_0 indicates that the holes are majority charge carriers in the whole temperature range.

In order to investigate the origin of AHE, we analyzed the ρ_{AH} versus ρ_{xx} on a double logarithmic scale. A linear fitting was employed to determine the exponent β according to the scaling relation $\rho_{\text{AH}} \propto \rho_{\text{xx}}{}^{\beta}$ [61,63] shown in Fig. 3(d). The exponent β decides the dependency of ρ_{AH} on ρ_{xx}. According to the well established theory of AHE, $\beta = 1$ is for the AHE that originates from the skew scattering mechanism and $\beta = 2$ is for the AHE governed by the scattering independent mechanism [64]. By this procedure, we found the exponent $\beta = 1.75$, which indicates the Berry phase mechanism as a dominant contribution in AHE. To find the value of intrinsic AHC, we have plotted ρ_{AH} versus ρ_{xx} [inset of Fig. 3(d)] and fitted with equation

$$\rho_{\text{AH}} = a\rho_{\text{xx}} + b\rho_{\text{xx}}{}^2. \tag{1}$$

Here a and b are the skew scattering coefficient and intrinsic AHC, respectively. By this, we found $a = 0.0004$ and intrinsic AHC $b \sim 78$ S/cm. The AHC due to the extrinsic side jump contribution is usually of the order of $e^2/hc(\epsilon_{\text{SOC}}/E_{\text{F}})$, where ϵ_{SOC} and E_{F} are the spin-orbit interaction energy and Fermi energy, respectively [65]. For metallic ferromagnets $\epsilon_{\text{SOC}}/E_{\text{F}}$ is generally less than 10^{-2} [61,66] and hence the side jump contribution in AHC is too small or negligible in comparison to intrinsic AHC. Further, to understand the microscopic origin of AHE, we need to look towards the variation of AHC with temperature and/or longitudinal resistivity. For this, we calculated Hall conductivity using the tensor conversion formula

$$\sigma_{\text{H}} = \frac{\rho_{\text{H}}}{(\rho_{\text{xx}}{}^2 + \rho_{\text{H}}{}^2)}. \tag{2}$$

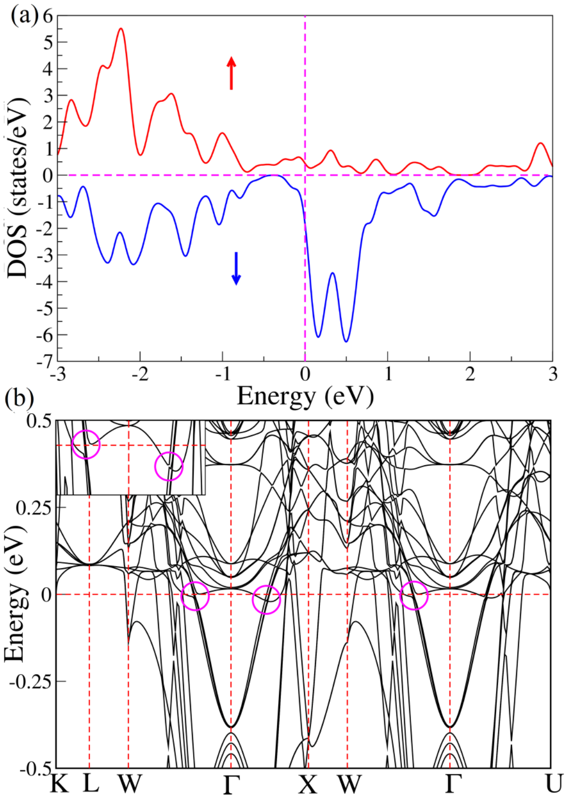

FIG. 5. (a) Total density of state (DOS) of Co$_2$FeGe for on site Coulomb interaction $U = 0$. Red and blue curves represent the total DOS for majority and minority spins. (b)The band structure of Co$_2$FeGe in the presence of SOC (gapped nodal lines are shown in circle and inset shows the enlarged view around the gapped nodal line).

Figure 4(a) displays the field dependent Hall conductivity curves at indicated temperatures. The AHC was calculated by zero field extrapolation of high field Hall conductivity data on the y axis and found close to 100 S/cm at room temperature. Figure 4(b) shows variation of longitudinal conductivity and AHC with temperature. AHC is nearly insensitive to temperature from several K to 300 K, while the longitudinal resistivity shows explicit temperature dependence, fairly indicating the origin of AHE governed by the intrinsic mechanism [63,67,68]. Since the intrinsic AHE merely depends on the band structure of material in order to get a better understanding of the origin of intrinsic AHE, we carried out a first principles calculation on Co$_2$FeGe.

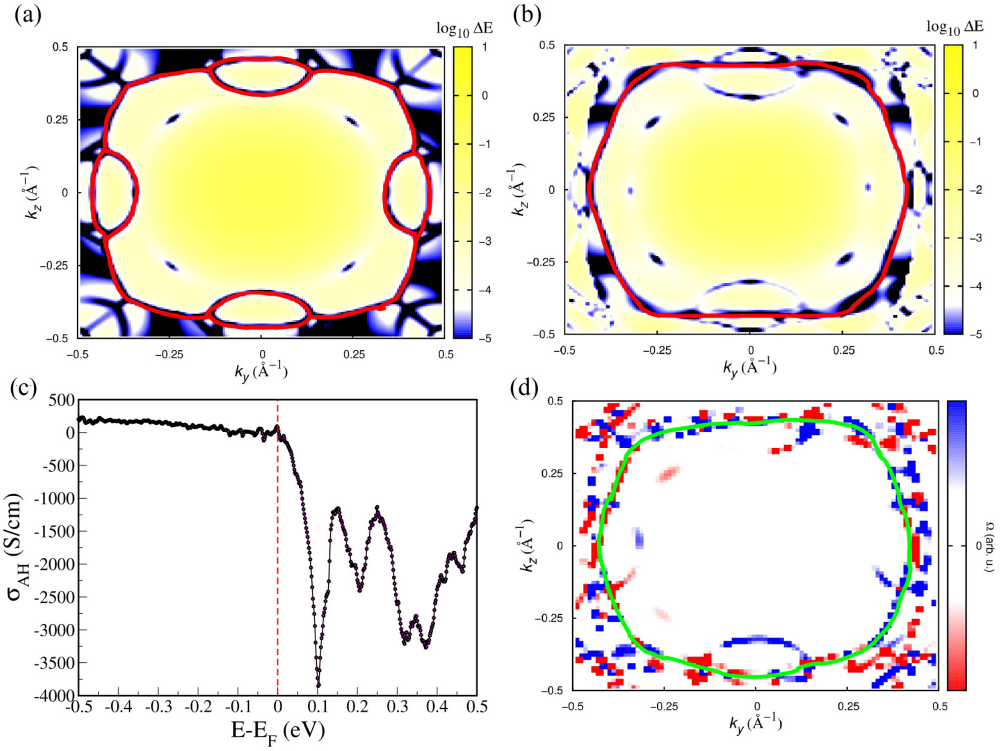

FIG. 6. Energy gap $\Delta E(k_y, k_z)$ is plotted in k_y-k_z plane at $k_x = 0$ (a) without SOC and (b) with SOC. Solid red lines represent gapless regions. (c) Energy ($E - E_F$) dependence of the AHC. (d) Berry curvature distribution in k_y-k_z plane at $k_x = 0$. Solid green lines represent gapless regions.

D. First principles calculation

Our *ab initio* calculation for a magnetic moment suggests that Fe and Co have a large magnetic moment with $\mu_{Fe} = 2.84\mu_B$/f.u. and $\mu_{Co} = 1.34\mu_B$/f.u., respectively, whereas Ge has a small vanishing magnetic moment. The total magnetic moment per formula unit is $5.53\mu_B$, aligned along the (001) direction, and the *d* orbital of the transition atoms Fe and Co are the major contributors. The magnetic moment of full Heusler alloys generally follows the Slater Pauling (SP) rule [69]; $M = Z - 24$, where M and Z are magnetic moments and the number of valance electrons, if the E_F lies in the band gap of the minority spin states. For Co$_2$FeGe, as per the SP rule the total magnetic moment should be $6\mu_B$/f.u. In some cases these systems may have gapless minority bands or minority bands crossing the E_F; then a small deviation in total magnetic moment from the SP rule may be expected [69]. The calculated magnetic moment for Co$_2$FeGe is in good agreement with the experimental value ($5.38\mu_B$/f.u.), but this value is smaller than that predicted by the SP rule. To understand the deviation of the magnetic moment total density of state (DOS) is calculated and shown in Fig. 5(a). Total DOS of minority spin electrons have finite value at E_F, which indicates presence of gapless states at the E_F or bands crossing E_F. A similar finite value of total DOS at E_F is also reported in literature for on site Coulomb interaction $U = 0$ [55,70,71]. We also performed calculations considering on site Coulomb repulsion U: 1.92 and 1.8 for the Co and Fe, respectively [72], and the calculated value of the magnetic moment is $\approx 6.00\mu_B$/f.u., which overestimates relative to experimental value; however, the magnetic moment is in agreement with literature [54,55,71]. Therefore, we believe that $U = 0$ is a more suitable parameter to explain the experimental findings. A similar conclusion is also reported for other Co$_2$-based Heusler alloys [35,73].

This material is expected to show a nodal line due to three relevant mirror planes m$_x$(k$_x$ = 0), m$_y$(k$_y$ = 0), and m$_z$(k$_z$ = 0) in the absence of SOC [41]. In the presence of SOC the nodal lines will gap out according to the magnetization direction and introduce Berry curvature in the system [13,41]. To understand the topological aspects, the nodal lines in the electronic band structure are analyzed in the absence and presence of SOC. The band structure with SOC coupling is calculated from the DFT calculation shown in Fig. 5(b). The band crossings are gapped out just below or at the E_F due to perturbation of SOC and these tiny gaps are shown inside the circle.

We analyzed the spectrum of a tight binding model Hamiltonian calculated from the WANNIER90 [45,46] calculation with the help of WANNIERTOOL [47]. In Figs. 6(a) and 6(b), we have shown an energy gap between the lowest conduction band and the topmost valence band at the k$_x$ = 0 plane and gaps are shown on a logarithmic scale of a color plot in the absence as well as in the presence of SOC, respectively. The gaps smaller than 10^{-4} eV are considered to be gapless. We noticed that four semicircular nodal lines appear in the $k_y - k_z$ plane of the first Brillouin zone [Fig. 6(a)] and, in the presence of the SOC, the gapless semicircular nodal lines are gapped out [Fig. 6(b)]. This material shows an intrinsic AHC, which can be expressed within the framework of linear response theory of the Kubo formalism [48],

$$\sigma_{\alpha\beta} = -\frac{e^2}{\hbar}\sum_n \int \frac{d^3k}{(2\pi)^3}\Omega^n_{\alpha\beta}(k) f_n(k), \tag{3}$$

where Berry curvature Ω can be written as a sum over eigenstates [74]:

$$\Omega^n_{\alpha\beta} = i\sum_{n\neq n'} \frac{\langle n|\frac{\partial H}{\partial R^\alpha}|n'\rangle\langle n'|\frac{\partial H}{\partial R^\beta}|n\rangle - (\alpha\leftrightarrow\beta)}{(\epsilon_n-\epsilon_{n'})^2}. \tag{4}$$

Here $|n\rangle$, ϵ_n, and $\epsilon_{n'}$ are the energy eigenstate and eigenvalue of n and n' bands, respectively. H, f_n, and $\Omega^n_{\alpha\beta}$ are the Hamiltonian, Fermi distribution function, and Berry curvature, respectively. The $\Omega^n_{\alpha\beta}$ is related to the change of electronic wave function within the Brillouin zone. The detail of Berry curvature is in the Appendix.

In Fig. 6(d), local Berry curvature is shown in the $k_x = 0$ plane of the Brillouin zone. Intrinsic AHC is calculated using maximally localized Wannier orbitals using $101\times101\times101$ k grid. The intrinsic AHC is proportional to the Brillouin zone summation of the Berry curvature over all occupied states and can be calculated using Eq. (3). We notice that the major contribution of AHC comes from the neighborhood of nodal lines. The AHC as a function of $E - E_F$ is shown in Fig. 6(c). The calculated AHC value at E_F is found to be 77.29 S/cm, which well matches with the experimentally found intrinsic AHC 78.6 S/cm. We have also calculated the energy dependent AHC as shown in Fig. 6(c) and it is evident that Fermi level shift in Co_2FeGe will result into an increased AHC.

IV. CONCLUSIONS

In conclusion, we have experimentally investigated the AHE in the Co_2FeGe Heusler alloy and performed first principle calculations to understand the origin of intrinsic AHE. Experimentally AHC was found close to 100 S/cm at 300 K with an intrinsic contribution of 78.6 S/cm. Berry curvature calculations give AHC about 77.29 S/cm due to a magnetization induced gapped nodal line near the E_F, which is in good agreement with the experimentally calculated intrinsic AHC.

ACKNOWLEDGMENTS

S.S. thanks the Science and Engineering Research Board of India for financial support through the award of Ramanujan Fellowship (Grant No. SB/S2/RJN-015/2017) and the Early Career Research Award (Grant No. ECR/2017/003186) and UGC-DAE CSR, Indore for financial support through its "CRS" Scheme. G.K.S. acknowledges the DST-INSPIRE scheme for support through a fellowship. M.K. thanks DST for funding through Grant No. CRG/2020/000754.

APPENDIX

In the semiclassical limit, electrons moving in bands of the magnetic system require additional terms for the anomalous contribution to the conductivity and correction is done considering the wave packet rather than just particle movement [48]. The wave packet can be written as

$$W_{k_c,\mathbf{r}_c}(\mathbf{r},t) = \sum_k a_k(k_c,t)\psi_{nk}(\mathbf{r}), \tag{A1}$$

where $\psi_{nk}(\mathbf{r}) = e^{ik\cdot\mathbf{r}}u_n(\mathbf{r},k)$. A wave packet is strongly centered at k_c in the Brillouin zone. $\mathbf{r}_c$ is the spatial center position of a wave packet. Here, $\mathbf{r_c}$ is defined by

$$\mathbf{r}_c = \langle W_{k_c,\mathbf{r}_c}|\mathbf{r}|W_{k_c,\mathbf{r}_c}\rangle \tag{A2}$$

and $a_k(k_c,t)$, the phase of the weighting function, can be given as

$$a_k(k_c,t) = |a_k(k_c,t)|e^{i(k-k_c)\cdot\mathbf{A}_n(k_c)-ik\cdot\mathbf{r}_c}, \tag{A3}$$

$$\mathbf{A}_n(k_c) = i\int_{u.c.}\mathbf{d}^3r\, u_n^*(\mathbf{r},k_c)\nabla_k u_n(\mathbf{r},k_c). \tag{A4}$$

$\mathbf{A}_n(k_c)$ is the Berry connection. Using the wave packet of the equation, one can write the Lagrangian and thereafter anomalous velocity can be calculated solving the Lagrangian. Anomalous velocity can be given as [48]

$$v_n = \frac{e}{\hbar}E\times\Omega_n(k_c), \tag{A5}$$

where E is an electric field and $\Omega_n(k_c)$ is the Berry curvature. The Berry curvature of a solid-state material in the tight binding limit can be written as $\Omega_n(k) = \Omega^k_n(k) + \Omega^r_n(k)$. For nondegenerate energy bands, these are defined as

$$\Omega^k_n(k) = -i\sum_{m\neq n}\left[\frac{C^\dagger_n(k)\nabla_k H(k)C_m(k)}{(\epsilon_{nk}-\epsilon_{mk})^2}\right.$$
$$\left.\times C^\dagger_m(k)\nabla_k H(k)C_n(k)\right], \tag{A6}$$
$$\Omega^r_n(k) = \sum_{m\neq n}2\,\mathrm{Re}\left[\frac{C^\dagger_n(k)\nabla_k H(k)C_m(k)}{(\epsilon_{nk}-\epsilon_{mk})}\right.$$
$$\left.\times C^\dagger_m(k)\mathbf{r}C_n(k)\right], \tag{A7}$$

where ϵ_{nk} and C^n_k are the energy of the nth band and the coefficient of the wave function, respectively. $H(k)$ is a Hamiltonian. However, for the degenerate band, $\Omega_n(k_c)$ can be calculated as in Eqs. (73) and (74) of Ref. [48].

---

[1] S. Wang, B.-C. Lin, A.-Q. Wang, D.-P. Yu, and Z.-M. Liao, Quantum transport in Dirac and Weyl semimetals: A review, Adv. Phys.: X **2**, 518 (2017).

[2] N. Nagaosa, T. Morimoto, and Y. Tokura, Transport, magnetic and optical properties of Weyl materials, Nat. Rev. Mater. **5**, 621 (2020).

[3] B. Yan and C. Felser, Topological materials: Weyl semimetals, Annu. Rev. Condens. Matter Phys. **8**, 337 (2017).

[4] D. Hsieh, Y. Xia, L. Wray, D. Qian, A. Pal, J. Dil, J. Osterwalder, F. Meier, G. Bihlmayer, C. Kane *et al.*, Observation of unconventional quantum spin textures in topological insulators, Science **323**, 919 (2009).

[5] J.-L. Xu, Y.-J. Sun, J.-L. He, Y. Wang, Z.-J. Zhu, Z.-Y. You, J.-F. Li, M. M. Chou, C.-K. Lee, and C.-Y. Tu, Ultrasensitive nonlinear absorption response of large-size topological insulator and application in low-threshold bulk pulsed lasers, Sci. Rep. **5**, 14856 (2015).

[6] P. Hosur and X. Qi, Recent developments in transport phenomena in Weyl semimetals, C. R. Phys. **14**, 857 (2013).

[7] B. Q. Lv, T. Qian, and H. Ding, Experimental perspective on three-dimensional topological semimetals, Rev. Mod. Phys. **93**, 025002 (2021).

[8] M. J. Klein, On a degeneracy theorem of kramers, Am. J. Phys. **20**, 65 (1952).

[9] T. Chen, T. Tomita, S. Minami, M. Fu, T. Koretsune, M. Kitatani, I. Muhammad, D. Nishio-Hamane, R. Ishii, F. Ishii *et al.*, Anomalous transport due to Weyl fermions in the chiral antiferromagnets Mn_3X, (X= Sn, Ge), Nat. Commun. **12**, 572 (2021).

[10] A. Burkov, Topological semimetals, Nat. Mater. **15**, 1145 (2016).

[11] S. A. Yang, Dirac and Weyl materials: Fundamental aspects and some spintronics applications, in *Spin* (World Scientific, Singapore, 2016), Vol. 6, p. 1640003.

[12] M. V. Berry, Quantal phase factors accompanying adiabatic changes, Proc. R. Soc. A: Math. Phys. Sci. **392**, 45 (1984).

[13] K. Manna, Y. Sun, L. Muechler, J. Kübler, and C. Felser, Heusler, Weyl and Berry, Nat. Rev. Mater. **3**, 244 (2018).

[14] K. Manna, L. Muechler, T.-H. Kao, R. Stinshoff, Y. Zhang, J. Gooth, N. Kumar, G. Kreiner, K. Koepernik, R. Car *et al.*, From Colossal to Zero: Controlling the Anomalous Hall Effect in Magnetic Heusler Compounds via Heusler Curvature Design, Phys. Rev. X **8**, 041045 (2018).

[15] J. Noky, J. Gooth, C. Felser, and Y. Sun, Characterization of topological band structures away from the Fermi level by the anomalous Nernst effect, Phys. Rev. B **98**, 241106(R) (2018).

[16] S.-Y. Xu, I. Belopolski, N. Alidoust, M. Neupane, G. Bian, C. Zhang, R. Sankar, G. Chang, Z. Yuan, C.-C. Lee *et al.*, Discovery of a Weyl fermion semimetal and topological Fermi arcs, Science **349**, 613 (2015).

[17] L. Yang, Z. Liu, Y. Sun, H. Peng, H. Yang, T. Zhang, B. Zhou, Y. Zhang, Y. Guo, M. Rahn *et al.*, Weyl semimetal phase in the non-centrosymmetric compound TaAs, Nat. Phys. **11**, 728 (2015).

[18] B. Lv, N. Xu, H. Weng, J. Ma, P. Richard, X. Huang, L. Zhao, G. Chen, C. Matt, F. Bisti *et al.*, Observation of Weyl nodes in TaAs, Nat. Phys. **11**, 724 (2015).

[19] Y. Sun, Y. Zhang, C. Felser, and B. Yan, Strong Intrinsic Spin Hall Effect in the TaAs Family of Weyl Semimetals, Phys. Rev. Lett. **117**, 146403 (2016).

[20] S.-Y. Xu, I. Belopolski, D. S. Sanchez, C. Zhang, G. Chang, C. Guo, G. Bian, Z. Yuan, H. Lu, T.-R. Chang *et al.*, Experimental discovery of a topological Weyl semimetal state in TaP, Sci. Adv. **1**, e1501092 (2015).

[21] A. A. Soluyanov, D. Gresch, Z. Wang, Q. Wu, M. Troyer, X. Dai, and B. A. Bernevig, Type-II Weyl semimetals, Nature (London) **527**, 495 (2015).

[22] Y. Sun, S.-C. Wu, M. N. Ali, C. Felser, and B. Yan, Prediction of Weyl semimetal in orthorhombic $MoTe_2$, Phys. Rev. B **92**, 161107(R) (2015).

[23] J. Liu and D. Vanderbilt, Weyl semimetals from noncentrosymmetric topological insulators, Phys. Rev. B **90**, 155316 (2014).

[24] P. Li, J. Koo, W. Ning, J. Li, L. Miao, L. Min, Y. Zhu, Y. Wang, N. Alem, C.-X. Liu *et al.*, Giant room temperature anomalous Hall effect and tunable topology in a ferromagnetic topological semimetal Co_2MnAl, Nat. Commun. **11**, 3476 (2020).

[25] A. A. Zyuzin, S. Wu, and A. A. Burkov, Weyl semimetal with broken time reversal and inversion symmetries, Phys. Rev. B **85**, 165110 (2012).

[26] D. Destraz, L. Das, S. S. Tsirkin, Y. Xu, T. Neupert, J. Chang, A. Schilling, A. G. Grushin, J. Kohlbrecher, L. Keller *et al.*, Magnetism and anomalous transport in the Weyl semimetal PrAlGe: possible route to axial gauge fields, npj Quantum Mater. **5**, 5 (2020).

[27] E. Liu, Y. Sun, N. Kumar, L. Muechler, A. Sun, L. Jiao, S.-Y. Yang, D. Liu, A. Liang, Q. Xu *et al.*, Giant anomalous Hall effect in a ferromagnetic kagome-lattice semimetal, Nat. Phys. **14**, 1125 (2018).

[28] X. Wan, A. M. Turner, A. Vishwanath, and S. Y. Savrasov, Topological semimetal and Fermi arc surface states in the electronic structure of pyrochlore iridates, Phys. Rev. B **83**, 205101 (2011).

[29] K. Ueda, R. Kaneko, H. Ishizuka, J. Fujioka, N. Nagaosa, and Y. Tokura, Spontaneous Hall effect in the Weyl semimetal candidate of all-in all-out pyrochlore iridate, Nat. Commun. **9**, 3032 (2018).

[30] K. S. Takahashi, H. Ishizuka, T. Murata, Q. Y. Wang, Y. Tokura, N. Nagaosa, and M. Kawasaki, Anomalous Hall effect derived from multiple Weyl nodes in high-mobility $EuTiO_3$ films, Sci. Adv. **4**, eaar7880 (2018).

[31] S. Borisenko, D. Evtushinsky, Q. Gibson, A. Yaresko, K. Koepernik, T. Kim, M. Ali, J. van den Brink, M. Hoesch, A. Fedorov *et al.*, Time-reversal symmetry breaking type-II Weyl state in $YbMnBi_2$, Nat. Commun. **10**, 3424 (2019).

[32] K. Kuroda, T. Tomita, M.-T. Suzuki, C. Bareille, A. Nugroho, P. Goswami, M. Ochi, M. Ikhlas, M. Nakayama, S. Akebi *et al.*, Evidence for magnetic Weyl fermions in a correlated metal, Nat. Mater. **16**, 1090 (2017).

[33] W. Luo, Y. Nakamura, J. Park, and M. Yoon, Cobalt-based magnetic Weyl semimetals with high-thermodynamic stabilities, npj Comput. Mater. **7**, 2 (2021).

[34] I. Belopolski, K. Manna, D. S. Sanchez, G. Chang, B. Ernst, J. Yin, S. S. Zhang, T. Cochran, N. Shumiya, H. Zheng *et al.*, Discovery of topological Weyl fermion lines and drumhead surface states in a room temperature magnet, Science **365**, 1278 (2019).

[35] G. Chang, S.-Y. Xu, H. Zheng, B. Singh, C.-H. Hsu, G. Bian, N. Alidoust, I. Belopolski, D. S. Sanchez, S. Zhang *et al.*, Room-temperature magnetic topological Weyl fermion and nodal line semimetal states in half-metallic Heusler $Co_2TiX(X = \mathrm{Si,\ Ge,\ or\ Sn})$, Sci. Rep. **6**, 38839 (2016).

[36] M. Hirschberger, S. Kushwaha, Z. Wang, Q. Gibson, S. Liang, C. A. Belvin, B. A. Bernevig, R. J. Cava, and N. P. Ong, The chiral anomaly and thermopower of Weyl fermions in the half-Heusler GdPtBi, Nat. Mater. **15**, 1161 (2016).

[37] W. Shi, L. Muechler, K. Manna, Y. Zhang, K. Koepernik, R. Car, J. van den Brink, C. Felser, and Y. Sun, Prediction of a magnetic Weyl semimetal without spin-orbit coupling and strong anomalous Hall effect in the Heusler compensated ferrimagnet Ti_2MnAl, Phys. Rev. B **97**, 060406(R) (2018).

[38] R. P. Dulal, B. R. Dahal, A. Forbes, N. Bhattarai, I. L. Pegg, and J. Philip, Weak localization and small anomalous Hall conduc-

tivity in ferromagnetic Weyl semimetal Co_2TiGe, Sci. Rep. **9**, 3342 (2019).

[39] B. Ernst, R. Sahoo, Y. Sun, J. Nayak, L. Müchler, A. K. Nayak, N. Kumar, J. Gayles, A. Markou, G. H. Fecher, and C. Felser, Anomalous Hall effect and the role of Berry curvature in Co_2TiSn Heusler films, Phys. Rev. B **100**, 054445 (2019).

[40] S. N. Guin, K. Manna, J. Noky, S. J. Watzman, C. Fu, N. Kumar, W. Schnelle, C. Shekhar, Y. Sun, J. Gooth *et al.*, Anomalous Nernst effect beyond the magnetization scaling relation in the ferromagnetic Heusler compound Co_2MnGa, NPG Asia Mater. **11**, 16 (2019).

[41] J. Noky, Y. Zhang, J. Gooth, C. Felser, and Y. Sun, Giant anomalous Hall and Nernst effect in magnetic cubic Heusler compounds, npj Comput. Mater. **6**, 77 (2020).

[42] D.-C. Tsai and C.-H. Chiang, Vacuum arc melting processes for biomedical NiTi shape memory alloy, in *MATEC Web of Conferences* (EDP Sciences, Les Ulis, 2015), Vol. 30, p. 01004.

[43] J. Hafner, Ab-initio simulations of materials using vasp: Density-functional theory and beyond, J. Comput. Chem. **29**, 2044 (2008).

[44] P. E. Blöchl, Projector augmented-wave method, Phys. Rev. B **50**, 17953 (1994).

[45] G. Pizzi, V. Vitale, R. Arita, S. Blügel, F. Freimuth, G. Géranton, M. Gibertini, D. Gresch, C. Johnson, T. Koretsune, J. Ibañez-Azpiroz, H. Lee, J.-M. Lihm, D. Marchand, A. Marrazzo, Y. Mokrousov, J. I. Mustafa, Y. Nohara, Y. Nomura, L. Paulatto *et al.*, Wannier90 as a community code: New features and applications, J. Phys.: Condens. Matter **32**, 165902 (2020).

[46] N. Marzari and D. Vanderbilt, Maximally localized generalized Wannier functions for composite energy bands, Phys. Rev. B **56**, 12847 (1997).

[47] Q. Wu, S. Zhang, H.-F. Song, M. Troyer, and A. A. Soluyanov, Wanniertools: An open-source software package for novel topological materials, Comput. Phys. Commun. **224**, 405 (2018).

[48] M. Gradhand, D. V. Fedorov, F. Pientka, P. Zahn, I. Mertig, and B. L. Györffy, First-principle calculations of the Berry curvature of Bloch states for charge and spin transport of electrons, J. Phys.: Condens. Matter **24**, 213202 (2012).

[49] J. Rodríguez-Carvajal, FULLPROF, a Rietveld and pattern matching and analysis programs version 2016, Laboratoire Leon Brillouin, CEA-CNRS, France, http://www.ill.eu/sites/fullprof/.

[50] Y. Takamura, R. Nakane, and S. Sugahara, Analysis of $L2_1$ ordering in full Heusler Co_2FeSi alloy thin films formed by rapid thermal annealing, J. Appl. Phys. **105**, 07B109 (2009).

[51] Y. Sakuraba, K. Hyodo, A. Sakuma, and S. Mitani, Giant anomalous Nernst effect in the $Co_2MnAl_{1-x}Si_x$ Heusler alloy induced by Fermi level tuning and atomic ordering, Phys. Rev. B **101**, 134407 (2020).

[52] S. Wurmehl, G. H. Fecher, H. C. Kandpal, V. Ksenofontov, C. Felser, and H.-J. Lin, Investigation of Co_2FeSi, the Heusler compound with highest Curie temperature and magnetic moment, Appl. Phys. Lett. **88**, 032503 (2006).

[53] B. Balke, S. Wurmehl, G. H. Fecher, C. Felser, M. d. C. M. Alves, F. Bernardi, and J. Morais, Structural characterization of the $Co_2FeZ(Z = Al, Si, Ga, \text{and } Ge)$ Heusler compounds by x-ray diffraction and extended x-ray absorption fine structure spectroscopy, Appl. Phys. Lett. **90**, 172501 (2007).

[54] B. Balke, S. Wurmehl, G. H. Fecher, C. Felser, and J. Kübler, Rational design of new materials for spintronics: Co_2FeZ (Z= Al, Ga, Si, Ge), Sci. Technol. Adv. Mater. **9**, 014102 (2008).

[55] D. Rai, A. Shankar, M. Ghimire, R. Thapa *et al.*, A comparative study of a Heusler alloy Co_2FeGe using LSDA and LSDA+U, Phys. B: Condens. Matter **407**, 3689 (2012).

[56] S. Amari, F. Dahmane, S. B. Omran, B. Doumi, I. Yahiaoui, A. Tadjer, and R. Khenata, Theoretical investigation of the structural, magnetic and band structure characteristics of $Co_2FeGe_{1-x}Si_x$ (x = 0, 0.5, 1) full-Heusler alloys, J. Korean Phys. Soc. **69**, 1462 (2016).

[57] D. Goodings, Electrical resistivity of ferromagnetic metals at low temperatures, Phys. Rev. **132**, 542 (1963).

[58] A. Markou, D. Kriegner, J. Gayles, L. Zhang, Y.-C. Chen, B. Ernst, Y.-H. Lai, W. Schnelle, Y.-H. Chu, Y. Sun, and C. Felser, Thickness dependence of the anomalous Hall effect in thin films of the topological semimetal Co_2MnGa, Phys. Rev. B **100**, 054422 (2019).

[59] I.-M. Imort, P. Thomas, G. Reiss, and A. Thomas, Anomalous Hall effect in the Co-based Heusler compounds Co_2FeSi and Co_2FeAl, J. Appl. Phys. **111**, 07D313 (2012).

[60] E. Vilanova Vidal, H. Schneider, and G. Jakob, Influence of disorder on anomalous Hall effect for Heusler compounds, Phys. Rev. B **83**, 174410 (2011).

[61] S. Roy, R. Singha, A. Ghosh, A. Pariari, and P. Mandal, Anomalous Hall effect in the half-metallic Heusler compound $Co_2TiX(X = Si, Ge)$, Phys. Rev. B **102**, 085147 (2020).

[62] N. Nagaosa, Anomalous Hall effect-A new perspective, J. Phys. Soc. Jpn. **75**, 042001 (2006).

[63] Q. Wang, Y. Xu, R. Lou, Z. Liu, M. Li, Y. Huang, D. Shen, H. Weng, S. Wang, and H. Lei, Large intrinsic anomalous Hall effect in half-metallic ferromagnet $Co_3Sn_2S_2$ with magnetic Weyl fermions, Nat. Commun. **9**, 3681 (2018).

[64] N. Nagaosa, J. Sinova, S. Onoda, A. H. MacDonald, and N. P. Ong, Anomalous Hall effect, Rev. Mod. Phys. **82**, 1539 (2010).

[65] I. Campbell and A. Fert, Transport properties of ferromagnets, *Handbook of Ferromagnetic Materials* (Elsevier, Amsterdam, 1982), Vol. 3, p. 747.

[66] Y. Liu, H. Tan, Z. Hu, B. Yan, and C. Petrovic, Anomalous Hall effect in the weak-itinerant ferrimagnet $FeCr_2Te_4$, Phys. Rev. B **103**, 045106 (2021).

[67] D. Liu, A. Liang, E. Liu, Q. Xu, Y. Li, C. Chen, D. Pei, W. Shi, S. Mo, P. Dudin *et al.*, Magnetic Weyl semimetal phase in a kagome crystal, Science **365**, 1282 (2019).

[68] X. Chen, M. Wang, C. Gu, S. Wang, Y. Zhou, C. An, Y. Zhou, B. Zhang, C. Chen, Y. Yuan *et al.*, Pressure-tunable large anomalous Hall effect of the ferromagnetic kagome-lattice Weyl semimetal $Co_3Sn_2S_2$, Phys. Rev. B **100**, 165145 (2019).

[69] S. V. Faleev, Y. Ferrante, J. Jeong, M. G. Samant, B. Jones, and S. S. P. Parkin, Unified explanation of chemical ordering, the Slater-Pauling rule, and half-metallicity in full Heusler compounds, Phys. Rev. B **95**, 045140 (2017).

[70] K. R. Kumar, K. K. Bharathi, J. A. Chelvane, S. Venkatesh, G. Markandeyulu, and N. Harishkumar, First-principles calculation and experimental investigations on full Heusler alloy Co_2FeGe, IEEE Trans. Magn. **45**, 3997 (2009).

[71] J.-M. Hyun and M. Kim, The half-metallicity of Co_2FeGe full Heusler alloy in (001) thin film:first principles study, J. Korean Phys. Soc. **72**, 276 (2018).

[72] K. Nawa and Y. Miura, Exploring half-metallic Co-based full Heusler alloys using a DFT + U method combined with linear response approach, RSC Adv. **9**, 30462 (2019).

[73] G. Chang, S.-Y. Xu, X. Zhou, S.-M. Huang, B. Singh, B. Wang, I. Belopolski, J. Yin, S. Zhang, A. Bansil *et al.*, Topological Hopf and Chain Link Semimetal States and their Application to Co_2MnGa, Phys. Rev. Lett. **119**, 156401 (2017).

[74] D. Xiao, M.-C. Chang, and Q. Niu, Berry phase effects on electronic properties, Rev. Mod. Phys. **82**, 1959 (2010).